JPhys Energy

Thermoelectric properties of organic thin films enhanced by *π*–*π* stacking

To cite this article: Xintai Wang *et al* 2022 *J. Phys. Energy* **4** 024002

IOP Publishing J. Phys. Energy 4 (2022) 024002 https://doi.org/10.1088/2515-7655/ac55a3

Journal of Physics: Energy

RECEIVED
7 October 2021

REVISED
8 February 2022

ACCEPTED FOR PUBLICATION
16 February 2022

PUBLISHED
23 March 2022

PAPER

Thermoelectric properties of organic thin films enhanced by π–π stacking

Xintai Wang[1,4], **Sara Sangtarash**[2], **Angelo Lamantia**[1], **Hervé Dekkiche**[3], **Leonardo Forcieri**[1], **Oleg V Kolosov**[1], **Samuel P Jarvis**[1], **Martin R Bryce**[3], **Colin J Lambert**[1], **Hatef Sadeghi**[2] **and Benjamin J Robinson**[1,*]

[1] Department of Physics, Lancaster University, Lancaster LA1 4YB, United Kingdom
[2] School of Engineering, University of Warwick, Coventry CV4 7AL, United Kingdom
[3] Department of Chemistry, Durham University, Durham DH1 3LE, United Kingdom
[4] School of Information Science and Technology, Dalian Maritime University, Liaoning 116026, People's Republic of China
[*] Author to whom any correspondence should be addressed.

E-mail: b.j.robinson@lancaster.ac.uk

Keywords: thermoelectric, molecules, thin-films, scanning probe micrscopy, nanomaterials, langmuir-blodgett, self-assembly

Supplementary material for this article is available online

Abstract

Thin films comprising synthetically robust, scalable molecules have been shown to have major potential for thermoelectric energy harvesting. Previous studies of molecular thin-films have tended to focus on massively parallel arrays of discrete but identical conjugated molecular wires assembled as a monolayer perpendicular to the electrode surface and anchored via a covalent bond, know as self-assembled monolayers. In these studies, to optimise the thermoelectric properties of the thin-film there has been a trade-off between synthetic complexity of the molecular components and the film performance, limiting the opportunities for materials integration into practical thermoelectric devices. In this work, we demonstrate an alternative strategy for enhancing the thermoelectric performance of molecular thin-films. We have built up a series of films, of controlled thickness, where the basic units—here zinc tetraphenylporphyrin—lie parallel to the electrodes and are linked via π–π stacking. We have compared three commonly used fabrications routes and characterised the resulting films with scanning probe and computational techniques. Using a Langmuir-Blodgett fabrication technique, we successfully enhanced the thermopower perpendicular to the plane of the ZnTPP multilayer film by a factor of 10, relative to the monolayer, achieving a Seebeck coefficient of $-65\ \mu\text{V K}^{-1}$. Furthermore, the electronic transport of the system, perpendicular to the plane of the films, was observed to follow the tunnelling regime for multi-layered films, and the transport efficiency was comparable with most conjugated systems. Furthermore, scanning thermal microscopy characterisation shows a factor of 7 decrease in thermal conductance with increasing film thickness from monolayer to multilayer, indicating enhanced thermoelectric performance in a π–π stacked junction.

1. Introduction

Thermoelectric devices, those that convert a heat flux to electric power [1], are attractive for a range of applications including energy generation and flexible sensors. Electricity is generated by the Seebeck effect and defined by the Seebeck coefficient, $S = -\Delta V/\Delta T$ where ΔV is the thermoelectric voltage generated in response to a temperature difference ΔT across the device. The overall thermoelectric efficiency is defined by a dimensionless figure of merit, $ZT = S^2GT/\kappa$ where G is the electrical conductance and κ is the thermal conductance across the device. Realising strategies for engineering high Seebeck coefficients has become one of the key challenges for thermoelectric devices.

Recently, it has been shown that small organic molecules, in both single-molecule junctions and large-area thin-films are promising candidates for fabricating thermoelectric devices, due to their low

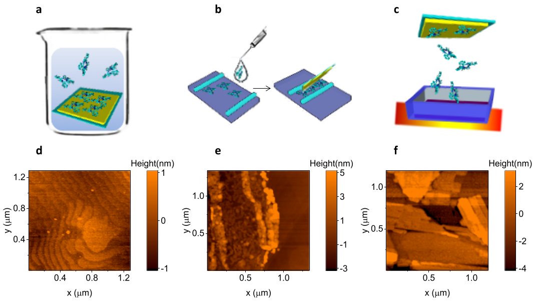

Figure 1. Scheme of ZnTPP thin film fabrication by (a) self-assembly, (b) Langmuir-Blodgett method and (c) thermal sublimation, and (d)–(f) corresponding AFM topographical images.

toxicity, ease of fabrication and electrical tunability through control of electrical transmission features relative to the position of the electrodes' Fermi energy [2–11]. Thus far, the investigated molecular junctions have largely focused on covalently linked components such as alkanes [12], oligo(phenylene)s [13], oligo(phenylene-ethynylene)s [14], and oligo(phenylene-vinylene)s [15]; non-covalent supra-molecular junctions comprising organic and 2D materials also show promise in both electrical [10, 16, 17] and thermal optimisation [7] of the junction. In addition to increasing the value of S, improvement in thermoelectric device performance can be achieved by reducing κ of the material; indeed, it has been predicted that the phononic contribution to thermal conductance in molecular junctions can be reduced by 95% via π–π stacking compared with that of covalently bonded systems [7], and this type of through-space π-conjugation can conduct electricity as efficient as conventional through-bond π-conjugations [18].

In this work, through both experimental and theoretical investigation, we demonstrate a new approach for enhancing the Seebeck coefficient of organic junctions, perpendicular to the plane of the organic film, through the π-stacking of a controlled number of molecular monolayers. Using Langmuir-Blodgett (LB) deposition, we fabricate and characterise multiple π-stacked molecular thin films, of controlled thickness, of zinc tetraphenylporphyrin (ZnTPP). Whilst ZnTPP is expected to give lower absolute values of S than recent reports for synthetically complex, tailored monolayer systems ($S \sim -250\ \mu\mathrm{V\ K^{-1}}$) [19], the molecule is known to have strong intra-stack π interactions [20–22] making it an ideal candidate for to demonstrate this new strategy for enhancing S. We compared the growth of the LB films to those obtained from self-assembled monolayers (SAMs), and thermal sublimation (figure 1). We obtain a room temperature Seebeck coefficient as high as $-65\ \mu\mathrm{V\ K^{-1}}$ in films of 4.8 nm thickness, an increase of a factor of ten from a monolayer SAM film. Our atomistic simulations using first principle methods show that this is due to the high slope of the transmission function close to the Fermi energy of the electrodes. These results promise great potential of stacked molecular structures for thermoelectricity.

2. Experimental

2.1. Synthesis

The free-base tetraphenylporphyrin (H_2TPP) was obtained by condensation of *p*-benzaldehyde and pyrrole in the presence of $BF_3.Et_2O$ in dichloromethane, as described by Lindsay *et al* [23]. Metallation with $Zn(OAc)_2$ provided ZnTPP following known experimental procedures [24]. The compound was purified by column chromatography and crystallised from dichloromethane/methanol. The characterisation data obtained for ZnTPP matched the previously reported data.

2.2. Molecular film growth

Three molecular film growth methodologies for ZnTPP were investigated. SAMs and LB films were grown on template striped gold (Au^{TS}) using a previously reported method [25, 26]. AFM was used to confirm Au^{TS} roughness <150 pm. The thicknesses of the molecular films were characterised by nano-scratching with an atomic force microscope (AFM) [27–29]. Thermally sublimed films were deposited on atomically clean Au(111) surfaces (Au(111):mica, Georg Albert PVD) prepared immediately prior to molecular deposition via *in-situ* sputter-annealing cycles carried out under UHV conditions.

SAMs were deposited by immersion of the Au^{TS} substrate in a 0.1 mM solution of ZnTPP in benzene as per established recipes [30–32]. Growth was monitored, in real-time, by a freshly cleaned Au coated quartz crystal microbalance (QCM) (openQCM Q-1, Novaetech Srl). The crystal was cleaned by oxygen plasma for 10 min, immersed in hot DMF (100 °C) for 2 h then room temperature DMF overnight, washed sequentially

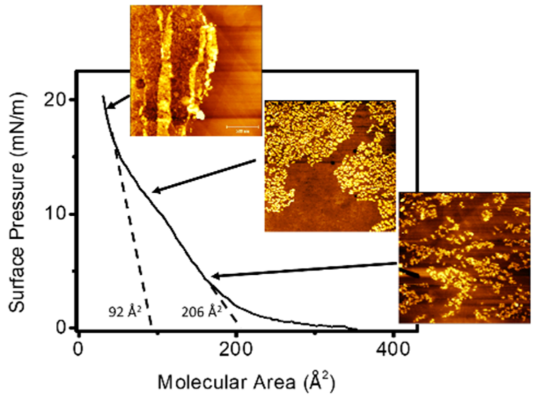

Figure 2. Langmuir-Blodgett isotherm of ZnTPP film on a water subphase with representative images of films transferred to Au^{TS} in different isotherm phases.

with ethanol and isopropanol, and dried in a vacuum oven for 20 h at 35 °C. A deposition time of 60 s resulted in a molecular density of the deposited film of $\sim$0.9 μmol m^{-2}, corresponding to 160 ± 20 Å^2 per molecule determined by a Sauerbrey analysis of the QCM response [33]. AFM nano-scratching showed a film thickness of $\sim$0.4 nm, in good agreement with the reported value for metallic porphyrin self-assembled on Au substrate (0.35–0.4 nm) [30]. QCM and nano-scratching indicated that the ZnTPP molecule is continuously adsorbed on the sample surface after monolayer formation. Further exposure of the deposited film to the ZnTPP solution was expected to result in multi-layered films due to favourable interaction between the zinc centre of one layer with the π-electrons of the pyrrole of the adjacent porphyrin layer(s) [30]. After 3 h of growth, the averaged film thickness was 1.3 ± 0.3 nm (corresponding to 3–4 layers of molecules), and the calculated molecular density on the surface was $\sim$2.7 μmol m^{-2}, 3 times higher than at the monolayer stage. The film thickness and the molecular density were observed to be the same after 12 h growth as after 3 h growth (figure S1, supplementary material available online at stacks.iop.org/JPEnergy/4/024002/mmedia) suggesting that 3–4 ZnTPP layers is the maximum achieved film thickness using this method.

LB films were prepared by spreading 150 μl of dilute (0.2 mg ml^{-1}) ZnTPP in toluene solution onto the pure water subphase of a KSV Nima LB trough (KN2003, Biolin Scientific). After allowing 10 min for the solvent to evaporate, the floating monolayers were compressed at 5 mm min^{-1}. The pressure–area (p–A) isotherm showed clear phase transitions at surface pressures of 4.8 mN m^{-1} and 12.5 mN m^{-1} corresponding to molecular occupation areas of 92 Å^2 and 206 Å^2, respectively (figure 2).

The thickness of the deposited film at 4.8 mN m^{-1} was 1.3 ± 0.2 nm (figure S2), and the film was discontinuous ($\sim$50% of the substrate surface was covered by the film). Further increase in the surface pressure and initial solvent volume lead to both better continuity and greater film thickness (figure 2, inserts); $\sim$2.5 nm thick films were obtained at 18.5 mN m^{-1}. The film, after compression, was transferred onto Au^{TS} substrate by vertical dipping. A second deposition cycle on the transferred film resulted in multilayer films $\sim$5 nm thick.

Thermally sublimed samples were prepared using standard methods described in detail elsewhere [34] with a sputtering energy of 0.6 keV at an Ar gas pressure of 5×10^{-6} mbar, followed by thermal annealing at 500 °C for 30 min, and a slow cool-down of $\sim$1 °C s^{-1}, obtaining an atomically flat surface and the well-known herringbone reconstruction. Zinc-tetraphenylporphyrin (ZnTPP) samples were grown under UHV conditions at a pressure lower than 1×10^{-9} mbar. The molecules were thermally sublimed at a temperature of 485 ± 20 K using a home-built glass evaporator designed for porphyrin deposition [34, 35]. Temperature was measured using a k-type thermocouple that was melted into the base of the crucible. The deposition rate was measured using a QCM and confirmed by subsequent AFM scans. The deposition cell consisted of a borosilicate crucible heated via a tightly coiled tantalum wire. Molecules were degassed prior to deposition via heating to a temperature 25 K higher than that used for sample preparation. Molecular layer thickness, from monolayer ($\sim$0.4 nm) to >10 layers ($\sim$5 nm), was controlled by the varying deposition time and correlating with the AFM images. Due to the atomically flat nature of the Au(111) surface, ZnTPP layers were easily identifiable by their increased layer height and square island shape (figure S3).

2.3. AFM nano-scratching

Initial film topography images were obtained by AFM (Multi-Mode 8, Bruker Nano Surfaces) operating in peak force mode. Nano-scratching was performed in contact mode at high set force ($F = 15$–40 nN) using a soft probe (Multi-75 G, $k = 3$ N m^{-1}) to 'sweep away' the molecules from a defined area. The topography of the sample after scratching was again characterized in peak force mode, the scratched window was easily observed. Nano-scratching was also conducted on a bare gold sample under the same conditions to ensure no gold was scratched away in the used force range. The height difference between the scratched part and un-scratched part indicates the thickness of the film.

2.4. Electrical characterisation

The electrical conductivity perpendicular to the plane of the film was characterized by a conductive AFM (cAFM) setup based on a Multi-mode 8 AFM instrument (Bruker Nano Surfaces). The bottom gold substrate was used as the source, and a Pt/Cr coated probe (Multi75 E, BugetSensors) was used as the drain. The force between the probe and the monolayer was controlled by the deflection error set point. The triangular shape AC bias was added between the source and drain by a voltage generator (Aglient 33500B), the source to drain current was acquired by a current pre-amplifier (DLPCA200, Femto) providing current-to-voltage conversion. The I–V characteristics were obtained by Nanoscope 8 controller simultaneously collecting drive bias and current with subsequent correlation of these values at each time point.

2.5. Thermopower characterisation

The Seebeck coefficient of the SAMs was obtained through use of Thermal-Electrical Atomic Force Microscopy (THEFM)[36–40], which is a modified version of the cAFM used for our electrical transport measurements. The probe was coated with 100 nm Au by thermal evaporation for voltage stabilisation. A Peltier stage controlled by a voltage generator (Agilent 33500B with buffer amplifier) was used for substrate temperature control, and a temperature difference between the sample and the probe, ΔT, can be created. A Type T thermal couple was used to quantify this ΔT. The thermal voltage between sample and probe, $\Delta V_{\mathrm{Therm}}$, was detected via a high impedance differential pre-amplifier (SR551, Standford Research System). The signal was passed through a low pass filter and recorded by the AFM controller. The linear regression of $\Delta V_{\mathrm{Therm}}$ vs. ΔT was plotted, and the slope of the linear curve was the Seebeck coefficient of the system (figures S4–S6).

2.6. Thermal characterisation

Ambient scanning thermal microscopy (SThM) measurements were performed using a standard contact AFM setup (Bruker Multi-Mode, Nanoscope III) with 'half-moon' SThM probe holder (Anasys Instruments) using a silicon nitride probe with Pd integrated heater (Kelvin Nanotechnologies). As the heated SThM tip is brought in contact with the surface some heat flows into the sample cooling the tip and hence changing the electrical resistance of the sensor. The probe's electrical resistance was calibrated as a function of applied voltage and temperature using the method described elsewhere [41], a linear dependence of the probe resistance on its temperature was always observed. In both ambient and vacuum cases, during measurement, the thermal probe represents part of a balanced Wheatstone electric bridge with a 4 $\mathrm{V_{AC}}$ drive at 91 kHz frequency and 2 $\mathrm{V_{DC}}$ bias, provided by a precision function generator (Model 3390, Keysight instruments), with the unbalance AC signal proportional to the probe temperature measured via lock-in amplifier (SRS-830, Stanford Research Systems). A constant power applied to the sensor generated Joule self-heating, enabling the tip temperature and the total probe thermal resistance to be acquired simultaneously. The thermal conductance of the measured film was estimated via the temperature change of the SThM probe [42].

2.7. Computational methods

The geometry of the structures studied in this paper was relaxed to the force tolerance of 10 meV Å^{-1} using the *SIESTA* [43] implementation of density functional theory (DFT), with a double-ζ polarized basis set and the generalized gradient approximation functional with Perdew–Burke–Ernzerhof parameterisation. A real-space grid was defined with an equivalent energy cut-off of 250 Ry.

To calculate the electronic properties of the device, from the converged DFT calculation, the underlying mean-field Hamiltonian H was combined with the quantum transport code, *Gollum* [44, 45]. This procedure yields the transmission coefficient $T_{\mathrm{el}}(E)$ for electrons of energy E (passing from the source to the drain) via the relation $T(E) = Tr\left(\Gamma_L(E)\, G^R(E)\, \Gamma_R(E)\, G^{R\dagger}(E)\right)$ where $\Gamma_{L,R}(E) = i\left(\sum_{L,R}(E) - \sum_{L,R}{}^{\dagger}(E)\right)$ describes the level broadening due to the coupling between left L and right R electrodes and the central scattering region, $\Gamma_{L,R}(E)$ are the retarded self-energies associated with this coupling and $G^R = \left(ES - H - \sum_L - \sum_R\right)^{-1}$ is the retarded Green's function, where H is the Hamiltonian and S is the overlap matrix obtained from *SIESTA* implementation of DFT. DFT+$\sum$ approach has been employed for spectral adjustment [45]. The electrical conductance $G(T) = G_0 L_0$, and the Seebeck coefficient $S(T) = -L_1/eTL_0$ are calculated from the electron transmission coefficient $T(E)$ where the momentums

$L_n(T) = \int_{-\infty}^{+\infty} \mathrm{d}E(E-E_\mathrm{F})^n T(E)\left(-\frac{\partial f(E,T)}{\partial E}\right)$ and $f(E,T)$ is the Fermi–Dirac probability distribution function $f(E,T) = \left(e^{(E-E_\mathrm{F})/k_\mathrm{B}T}+1\right)^{-1}$, T is the temperature, k_B is Boltzmann constant E_F is the Fermi energy, $G_0 = 2e^2/h$ is the conductance quantum, e is electron charge and h is the Planck's constant.

3. Results and discussion

Films fabricated by the three growth methods, collectively, spanned thicknesses from monolayer (0.4 nm) to ∼12–14 layers (4.8 nm). The film's electrical conductance was investigated by cAFM [46], the junction area was estimated via a Hertz model [36, 47, 48], and calibrated to single molecular occupation area (figures 3(a)–(c)). For films prepared by different methods, the electrical conductance ($\mathrm{d}I/\mathrm{d}V$) at near 0 bias was found to decay exponentially with film thickness, such that,

$$\ln(G) = \ln(G_\mathrm{C}) - \beta d$$

where G the measured conductance, G_C the contact conductance, β the attenuation factor of the junction, d the film thickness. Crucially, electron mobility does not need to be considered here as it is only relevant when electrons undergo inelastic scattering as they traverse the device. This would happen for transport within the plane, but does not occur for transport perpendicular to the plane, because the film thickness is too small (in the range 0.3–5 nm). Over such short distances, inelastic scattering is negligible and transport takes place via phase-coherent tunnelling. This is evidence by figure 3(d), which show that electrical conductance decays exponentially with length, which is a hall mark of tunnelling [12–14] (figure 3(d)).

The attenuation factor, β, indicates the electron transmission efficiency across the plane of the molecular thin film. This value was 3.7 nm^{-1}, 3.1 nm^{-1} and 2.9 nm^{-1} for SAMs, LB and thermally sublimed ZnTPP films respectively, which was significantly better than an aliphatic carbon system such as alkyl thiol based SAMs (7–10 nm^{-1})[12], and similar to other reported wires in conjugation (oligo(phenylene-ethynylene) $\sim 2\ \mathrm{nm}^{-1}$ [49], oligo(aryleneethynylene) $\sim 3.3\ \mathrm{nm}^{-1}$ [50], acene $\sim 3.1\ \mathrm{nm}^{-1}$ [51]). This means, despite the absence of covalent bonding between layers, the π stacking between ZnTPP maintains the electron transmission efficiency through the film at the same level to other commonly used molecular junction systems. The range of experimental β values observed is attributed to the increased disorder in the film structure due to both growth technique and increased thickness and is consistent with other studies of ZnTPP multilayers [21].

Thermopower of the thin film in this work was measured by ThEFM. For all films, the measured thermal voltage ($V_\mathrm{hot} - V_\mathrm{cold}$) increased positively with increase of temperature difference ($T_\mathrm{hot} - T_\mathrm{cold}$) (figures 4(a)–(c)) resulting in negative Seebeck coefficients of the junction and indicating that the Fermi level of the junction was located near the LUMO resonance of the molecule [1, 52, 53]. Crucially, for all films prepared by the different methods, linear relationships between film thickness and Seebeck coefficient were observed (figure 4(d)). This demonstrated the intermolecular coupling between porphyrin layers enhanced the thermopower of the junction [16]. The absolute Seebeck coefficients were found to depend on the film fabrication method. At comparable thickness (∼4.5 nm), the film prepared by the LB method ($-65 \pm 15\ \mu V\,K^{-1}$) was significantly higher than the thermally sublimed film ($-32 \pm 10\ \mu V\,K^{-1}$, figure 4(d)).

In agreement with previous studies [54], thermal conductance, as calculated from probe voltage changes during SThM approach—retract curves (e.g. figure 5(a)), indicates a monotonic decrease in thermal conductance with number of ZnTPP layers (figure 5(b)). This is predicted to indicate the suppression of phonon transport between π-stacked layers [7]. It is worth noting the difference between the thermal conductivity values for four layers of ZnTPP fabricated by LB and self-assembly as well as the greater decrease with layer number for SAMs both believed top indicate more ordered films from self-assembly than LB deposition. This is consistent with trends observed for the thermopower shown in figure 4.

To further understand the electronic and thermoelectric properties of the zinc porphyrins films (figure 6(a)) assembled in a junction, we computationally studied idealised molecular junctions consisting of layers (L) of stacked zinc porphyrins (ZnP) between gold electrodes [55, 56]. ZnP rather than ZnTPP were used here to reduce compuational time. The ground state mean field Hamiltonian of the junctions was obtained from their optimised geometry using SIESTA [43] implementation of DFT. The optimisation reveals that the ground state geometry corresponds to the porphyrin units stacked in the configuration shown in figure 6(a). We then combined the Hamiltonian with Gollum implementation of non-equilibrium Green's function method [44, 45] to obtain the transmission coefficient T of electrons with energy E passing from the top electrode to the bottom. Figure 6(b) shows the transmission coefficient of junctions with different numbers of porphyrin units between gold electrodes. Clearly, the transmission coefficient decreases

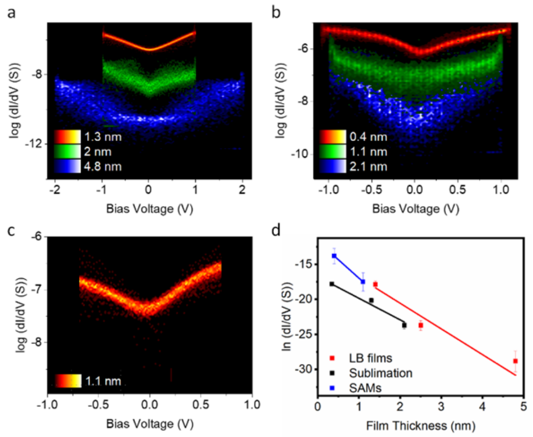

Figure 3. Electric conductance heat maps for ZnTPP films prepared by (a) LB, (b) thermal sublimation and (c) self Assembly (0.4 nm SAM's current was out of range), and (d) the dependence of conductance (in logarithmic scale) vs. film thickness.

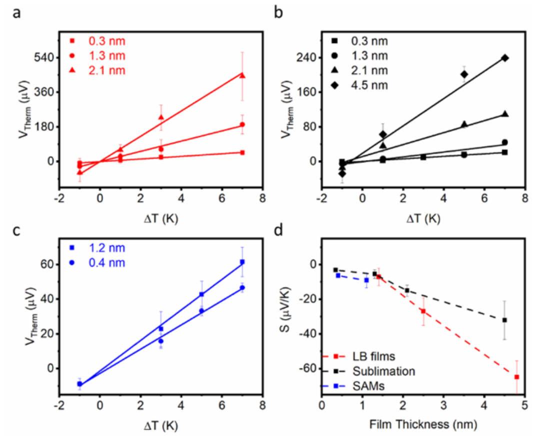

Figure 4. Thermal voltages vs. temperature difference for ZnTPP films of different thicknesses prepared by (a) LB, (b) thermal sublimation and (c) self assembly, and (d) Seebeck coefficient vs. film thickness of the different films.

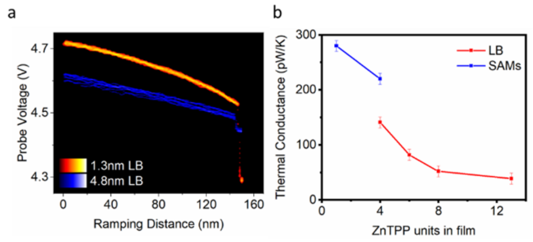

Figure 5. (a) Thermal conductance measurement on 1.3 nm and 4.8 nm LB film, a clear difference in probe voltage change was observed. (b) Plot of film thermal conductance vs. number of ZnTPP layer with different film preparation methods.

with the number of porphyrins. Figure 6(c) shows the average room temperature conductance versus the length of the junctions for a range of Fermi energies around the DFT Fermi energy. We found the decay attenuation factor of 3.7 nm^{-1} in agreement with the experimental observation of figure 3(d).

From the transmission coefficient, the Seebeck coefficient was obtained for each junction. Figure 6(d) shows the room temperature Seebeck coefficient for the junctions with different numbers of porphyrin units. The average Seebeck coefficient over a range of Fermi energies can be obtained using the relation [57] <S>=<GS>/<G> where G and S are the electrical conductance and Seebeck coefficient, respectively. Clearly, the average Seebeck coefficient for energies around the DFT Fermi energy (yellow region in figure 6(b)) increases with length and reaches high values of ca. $-150\ \mu\mathrm{V\ K}^{-1}$ at room temperature in the junctions with ten porphyrin units sandwiched between gold electrodes.

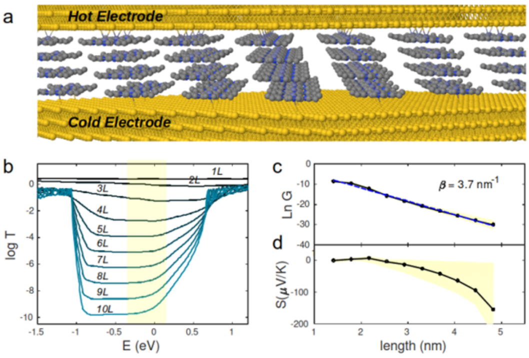

Figure 6. Transport through stacked porphyrins. (a) Example of molecular junctions with four layer stacked ZnP, (b) transmission coefficient of electrons passing from top electrode to the bottom one through 1–10 layers (L) of stacked ZnP, (c) conductance and (d) Seebeck coefficient versus the length of junctions.

Whilst noting the excellent agreement between the trends in conductance properties and Seebeck coefficients, we observe a discrepancy (∼50%) between the optimised, theoretical value of the Seebeck coefficient for the junctions and the experimental measurements. We believe this discrepancy comes from the non-idealised structure of the as-gown films which, in turn, introduces disorder into the junction, the extent of which increases with increasing film thickness [21].

4. Conclusions

We have demonstrated a successful strategy for increasing the Seebeck coefficient of molecular junctions using multi-layered ZnTPP films stabilised by inter-layer π–π stacking fabricated by three different growth techniques. The electronic transport of the system followed the tunnelling regime, and the transport efficiency was comparable with most conjugated systems. The Seebeck coefficient of the junction was proportional to the film thickness; this trend was observed up to the maximum film thickness fabricated of ∼4.5 nm. Moving from monolayer to multilayer ZnTPP junctions allowed us to engineering an increase in Seebeck coefficient of $\sim\times 10$ achieving $> -60\ \mu$V K^{-1} at room temperature whilst simultaneously decreasing the junction's thermal conductivity; this approach demonstrates an exciting new avenue to achieve high thermoelectric performance in simple, scalable materials.

Data availability statement

The data that support the findings of this study are available upon reasonable request from the authors.

Acknowledgments

The work in Durham was funded by EPSRC Grant Nos. EP/P027520/1 and EC H2020 FET Open projects: Grant Agreement Nos. 767187 'QuIET' and 766853 'EFINED'. The work at Lancaster was supported by EPSRC Grants EP/P027156/1 and EP/N03337X/, Graphene Flagship Core 3 project and, B R also acknowledges support from Royal Society Grant RG160834. H S acknowledges the UKRI for Future Leaders Fellowship No. MR/S015329/2. S S acknowledges the Leverhulme Trust for Early Career Fellowship No. ECF-2018-375. We are thankful to Chris Ford of the Cavendish Laboratory, University of Cambridge, UK for stimulating discussions.

ORCID iDs

Xintai Wang https://orcid.org/0000-0002-6151-414X
Sara Sangtarash https://orcid.org/0000-0003-1152-5673
Oleg V Kolosov https://orcid.org/0000-0003-3278-9643
Samuel P Jarvis https://orcid.org/0000-0003-4031-1519
Martin R Bryce https://orcid.org/0000-0003-2097-7823
Colin J Lambert https://orcid.org/0000-0003-2332-9610
Hatef Sadeghi https://orcid.org/0000-0001-5398-8620
Benjamin J Robinson https://orcid.org/0000-0001-8676-6469

References

[1] Reddy P, Jang S Y, Segalman R A and Majumdar A 2007 Thermoelectricity in molecular junctions *Science* **315** 1568–71

[2] Wang X T *et al* 2020 Scale-up of room-temperature constructive quantum interference from single molecules to self-assembled molecular-electronic films *J. Am. Chem. Soc.* **142** 8555–60

[3] Ismael A, Wang X T, Bennett T L R, Wilkinson L A, Robinson B J, Long N J, Cohen L F and Lambert C J 2020 Tuning the thermoelectrical properties of anthracene-based self-assembled monolayers *Chem. Sci.* **11** 6836–41

[4] Zhang Y and Park S J 2019 Flexible organic thermoelectric materials and devices for wearable green energy harvesting *Polymers* **11** 909

[5] Sangtarash S, Sadeghi H and Lambert C J 2018 Connectivity-driven bi-thermoelectricity in heteroatom-substituted molecular junctions *Phys. Chem. Chem. Phys.* **20** 9630–7

[6] Herrer I L, Ismael A K, Milań D C, Vezzoli A, Martín S, Gonzalez-Orive A, Grace I, Lambert C, Serrano J L and Nichols R J 2018 Unconventional single-molecule conductance behavior for a new heterocyclic anchoring group: pyrazolyl *J. Phys. Chem. Lett.* **9** 5364–72

[7] Li Q, Strange M, Duchemin I, Donadio D and Solomon G C 2017 A strategy to suppress phonon transport in molecular junctions using pi-stacked systems *J. Phys. Chem.* C **121** 7175–82

[8] Zhang Y and Park S J 2017 Enhanced interfacial interaction by grafting carboxylated-macromolecular chains on nanodiamond surfaces for epoxy-based thermosets *J. Polym. Sci.* **55** 1890–8

[9] Ismael A K, Wang K, Vezzoli A, Al-Khaykanee M K, Gallagher H E, Grace I M, Lambert C J, Xu B, Nichols R J and Higgins S J 2017 Side-group-mediated mechanical conductance switching in molecular junctions *Angew. Chem., Int. Ed.* **56** 15378–82

[10] Rincon-Garcia L, Ismael A K, Evangeli C, Grace I, Rubio-Bollinger G, Porfyrakis K, Agrait N and Lambert C J 2016 Molecular design and control of fullerene-based bi-thermoelectric materials *Nat. Mater.* **15** 289

[11] Al-Galiby Q H, Sadeghi H, Algharagholy L A, Grace I and Lambert C 2016 Tuning the thermoelectric properties of metallo-porphyrins *Nanoscale* **8** 2428–33

[12] Engelkes V B, Beebe J M and Frisbie C D 2004 Length-dependent transport in molecular junctions based on SAMs of alkanethiols and alkanedithiols: effect of metal work function and applied bias on tunneling efficiency and contact resistance *J. Am. Chem. Soc.* **126** 14287–96

[13] Wold D J, Haag R, Rampi M A and Frisbie C D 2002 Distance dependence of electron tunneling through self-assembled monolayers measured by conducting probe atomic force microscopy: unsaturated versus saturated molecular junctions *J. Phys. Chem.* B **106** 2813–6

[14] Wei Z M *et al* 2012 Molecular junctions based on SAMs of cruciform oligo(phenylene ethynylene)s *Langmuir* **28** 4016–23

[15] Moreno-Garcia P *et al* 2013 Single-molecule conductance of functionalized oligoynes: length dependence and junction evolution *J. Am. Chem. Soc.* **135** 12228–40

[16] Evangeli C, Gillemot K, Leary E, Gonzalez M T, Rubio-Bollinger G, Lambert C J and Agrait N 2013 Engineering the thermopower of C-60 molecular junctions *Nano Lett.* **13** 2141–5

[17] Almutlaq N, Al-Galiby Q, Bailey S and Lambert C J 2016 Identification of a positive-Seebeck-coefficient exohedral fullerene *Nanoscale* **8** 13597–602

[18] Chen H and Fraser Stoddart J 2021 From molecular to supramolecular electronics *Nat. Rev. Mater.* **6** 804–28

[19] Liu J *et al* 2020 N-type organic thermoelectrics: demonstration of ZT > 0.3 *Nat. Commun.* **11** 5694

[20] Conron S M M, Shoer L E, Smeigh A L, Ricks A B and Wasielewski M R 2013 Photoinitiated electron transfer in zinc porphyrin-perylenediimide cruciforms and their self-assembled oligomers *J. Phys. Chem.* B **117** 2195–204

[21] Zhang X L, Jiang J W, Liu Y T, Lou S T, Gao C L and Jin Q Y 2016 Identifying the assembly configuration and fluorescence spectra of nanoscale zinc-tetraphenylporphyrin aggregates with scanning tunneling microscopy *Sci. Rep.* **6** 22756

[22] Cai J H, Chen H H, Huang J G, Wang J X, Tian D L, Dong H L and Jiang L 2014 Controlled self-assembly and photovoltaic characteristics of porphyrin derivatives on a silicon surface at solid-liquid interfaces *Soft Matter* **10** 2612–8

[23] Lindsey J S, Schreiman I C, Hsu H C, Kearney P C and Marguerettaz A M 1987 Rothemund and Adler-Longo reactions revisited: synthesis of tetraphenylporphyrins under equilibrium conditions *J. Org. Chem.* **52** 827–36

[24] Bhyrappa P and Krishnan V 1991 Octabromotetraphenylporphyrin and its metal derivatives: electronic structure and electrochemical properties *Inorg. Chem.* **30** 239–45

[25] Weiss E A, Kaufman G K, Kriebel J K, Li Z, Schalek R and Whitesides G M 2007 Si/SiO$_2$-Templated formation of ultraflat metal surfaces on glass, polymer, and solder supports: their use as substrates for self-assembled monolayers *Langmuir* **23** 9686–94

[26] Banner L T, Richter A and Pinkhassik E 2009 Pinhole-free large-grained atomically smooth Au(111) substrates prepared by flame-annealed template stripping *Surf. Interface Anal.* **41** 49–55

[27] Garcia R, Martinez R V and Martinez J 2006 Nano-chemistry and scanning probe nanolithographies *Chem. Soc. Rev.* **35** 29–38

[28] Amro N A, Xu S and Liu G Y 2000 Patterning surfaces using tip-directed displacement and self-assembly *Langmuir* **16** 3006–9

[29] Kaholek M, Lee W K, LaMattina B, Caster K C and Zauscher S 2004 Fabrication of stimulus-responsive nanopatterned polymer brushes by scanning-probe lithography *Nano Lett.* **4** 373–6

[30] Yoshimoto S, Tsutsumi E, Suto K, Honda Y and Itaya K 2005 Molecular assemblies and redox reactions of zinc(II) tetraphenylporphyrin and zinc(II) phthalocyanine on Au(111) single crystal surface at electrochemical interface *Chem. Phys.* **319** 147–58

[31] Yoshimoto S, Tada A, Suto K, Narita R and Itaya K 2003 Adlayer structure and electrochemical reduction of O$_2$ on self-organized arrays of cobalt and copper tetraphenyl porphines on a Au(111) surface *Langmuir* **19** 672–7

[32] Yoshimoto S, Inukai J, Tada A, Abe T, Morimoto T, Osuka A, Furuta H and Itaya K 2004 Adlayer structure of and electrochemical O$_2$ reduction on cobalt porphine-modiried and cobalt octaethylporphyrin-modifled Au(111) in HClO$_4$ *J. Phys. Chem.* B **108** 1948–54

[33] Sauerbrey G 1959 Verwendung von Schwingquarzen zur Wagung Dunner Schichten und zur Mikrowagung *Z. Phys.* **155** 206–22

[34] Jarvis S P, Taylor S, Baran J D, Thompson D, Saywell A, Mangham B, Champness N R, Larsson J A and Moriarty P 2015 Physisorption controls the conformation and density of states of an adsorbed porphyrin *J. Phys. Chem.* C **119** 27982–94

[35] Jarvis S P, Taylor S, Baran J D, Champness N R, Larsson J A and Moriarty P 2015 Measuring the mechanical properties of molecular conformers *Nat. Commun.* **6** 8338

[36] O'Driscoll L J, Wang X, Jay M, Batsanov A S, Sadeghi H, Lambert C J, Robinson B J and Bryce M R 2020 Carbazole-based tetrapodal anchor groups for gold surfaces: synthesis and conductance properties *Angew. Chem., Int. Ed.* **59** 882–9

[37] Cui L J, Hur S, Akbar Z A, Klockner J C, Jeong W, Pauly F, Jang S Y, Reddy P and Meyhofer E 2019 Thermal conductance of single-molecule junctions *Nature* **572** 628

[38] Wei Z M *et al* 2015 Molecular heterojunctions of oligo(phenylene ethynylene)s with linear to cruciform framework *Adv. Funct. Mater.* **25** 1700–8

[39] Tan A, Balachandran J, Sadat S, Gavini V, Dunietz B D, Jang S Y and Reddy P 2011 Effect of length and contact chemistry on the electronic structure and thermoelectric properties of molecular junctions *J. Am. Chem. Soc.* **133** 8838–41

[40] Tan A, Sadat S and Reddy P 2010 Measurement of thermopower and current-voltage characteristics of molecular junctions to identify orbital alignment *Appl. Phys. Lett.* **96** 013110

[41] Robinson B J, Pumarol M E and Kolosov O V 2019 Correlation of shear forces and heat conductance in nanoscale junctions *Phys. Rev.* B **100** 235426

[42] Spiece J, Evangeli C, Lulla K, Robson A, Robinson B and Kolosov O 2018 Improving accuracy of nanothermal measurements via spatially distributed scanning thermal microscope probes *J. Phys. D: Appl. Phys.* **124** 015101

[43] Soler J M, Artacho E, Gale J D, García A, Junquera J, Ordejón P and Sánchez-Portal D 2002 The SIESTA method forab initioorder-Nmaterials simulation *J. Phys.: Condens. Matter* **14** 2745–79

[44] Ferrer J *et al* 2014 GOLLUM: a next-generation simulation tool for electron, thermal and spin transport *New J. Phys.* **16** 093029

[45] Sadeghi H 2018 Theory of electron, phonon and spin transport in nanoscale quantum devices *Nanotechnology* **29** 373001

[46] Engelkes V B, Beebe J M and Frisbie C D 2005 Analysis of the causes of variance in resistance measurements on metal-molecule-metal junctions formed by conducting-probe atomic force microscopy *J. Phys. Chem.* B **109** 16801–10

[47] Burnham N A, Colton R J and Pollock H M 1993 Work-function anisotropies as an origin of long-range surface forces—reply *Phys. Rev. Lett.* **70** 247

[48] Weihs T P, Nawaz Z, Jarvis S P and Pethica J B 1991 Limits of imaging resolution for atomic force microscopy of molecules *Appl. Phys. Lett.* **59** 3536–8

[49] Kaliginedi V, Moreno-Garcia P, Valkenier H, Hong W J, Garcia-Suarez V M, Buiter P, Otten J L H, Hummelen J C, Lambert C J and Wandlowski T 2012 Correlations between molecular structure and single-junction conductance: a case study with oligo(phenylene-ethynylene)-type wires *J. Am. Chem. Soc.* **134** 5262–75

[50] Zhao X T, Huang C C, Gulcur M, Batsanov A S, Baghernejad M, Hong W J, Bryce M R and Wandlowski T 2013 Oligo(aryleneethynylene)s with terminal pyridyl groups: synthesis and length dependence of the tunneling-to-hopping transition of single-molecule conductances *Chem. Mater.* **25** 4340–7

[51] Kim B, Beebe J M, Jun Y, Zhu X Y and Frisbie C D 2006 Correlation between HOMO alignment and contact resistance in molecular junctions: aromatic thiols versus aromatic isocyanides *J. Am. Chem. Soc.* **128** 4970–1

[52] Paulsson M and Datta S 2003 Thermoelectric effect in molecular electronics *Phys. Rev.* B **67** 241403

[53] Malen J A, Doak P, Baheti K, Tilley T D, Segalman R A and Majumdar A 2009 Identifying the length dependence of orbital alignment and contact coupling in molecular heterojunctions *Nano Lett.* **9** 1164–9

[54] Kiršanskas G, Li Q, Flensberg K, Solomon G C and Leijnse M 2014 Designing π-stacked molecular structures to control heat transport through molecular junctions *Appl. Phys. Lett.* **105** 233102

[55] Algethami N, Sadeghi H, Sangtarash S and Lambert C J 2018 The conductance of porphyrin-based molecular nanowires increases with length *Nano Lett.* **18** 4482–6

[56] Sadeghi H, Sangtarash S and Lambert C 2017 Robust molecular anchoring to graphene electrodes *Nano Lett.* **17** 4611–8

[57] Lambert C J, Sadeghi H and Al-Galiby Q H 2016 Quantum-interference-enhanced thermoelectricity in single molecules and molecular films *C. R. Phys.* **17** 1084–95